

Article

# Isolating an Outflow Component in Single-Epoch Spectra of Quasars

Paola Marziani <sup>1,\*</sup> , Alice Deconto-Machado <sup>2</sup>  and Ascension Del Olmo <sup>2</sup> <sup>1</sup> National Institute for Astrophysics (INAF), Astronomical Observatory of Padova, IT-35122 Padova, Italy<sup>2</sup> Instituto de Astrofísica de Andalucía, IAA-CSIC, Glorieta de la Astronomía s/n, E-18008 Granada, Spain; adeconto@iaa.es (A.D.-M.); chony@iaa.es (A.D.O.)

\* Correspondence: paola.marziani@inaf.it; Tel.: +39-0498293415

**Abstract:** Gaseous outflows appear to be a universal property of type-1 and type-2 active galactic nuclei (AGN). The main diagnostic is provided by emission features shifted to higher frequencies via the Doppler effect, implying that the emitting gas is moving toward the observer. However, beyond the presence of blueshift, the observational signatures of the outflows are often unclear, and no established criteria exist to isolate the outflow contribution in the integrated, single-epoch spectra of type-1 AGN. The emission spectrum collected the typical apertures of long-slit spectroscopy or of fiber optics sample contributions over a broad range of spatial scales, making it difficult to analyze the line profiles in terms of different kinematical components. Nevertheless, hundred of thousands of quasars spectra collected at moderate resolution demand a proper analysis of the line profiles for proper dynamical modeling of the emitting regions. In this small contribution, we analyze several profiles of the H $\beta$  Balmer line from composite and individual spectra of sources radiating at moderate Eddington ratio (Population B). Features and profile shapes that might be traced to outflow due to narrow-line region gas are detected over a wide range of luminosity.

**Keywords:** active galactic nuclei; optical spectroscopy; ionized gas; broad line region**Citation:** Marziani, P.;

Deconto-Machado, A.; Del Olmo, A.

Isolating an Outflow Component in  
Single-Epoch Spectra of Quasars.*Galaxies* **2022**, *10*, 54.[https://doi.org/10.3390/](https://doi.org/10.3390/galaxies10020054)[galaxies10020054](https://doi.org/10.3390/galaxies10020054)

Academic Editor: Santanu Mondal

Received: 15 February 2022

Accepted: 17 March 2022

Published: 24 March 2022

**Publisher's Note:** MDPI stays neutral with regard to jurisdictional claims in published maps and institutional affiliations.



**Copyright:** © 2022 by the authors. Licensee MDPI, Basel, Switzerland. This article is an open access article distributed under the terms and conditions of the Creative Commons Attribution (CC BY) license (<https://creativecommons.org/licenses/by/4.0/>).

## 1. Introduction

Type-1 active galactic nuclei (AGN) are characterized by the presence of broad and narrow optical and UV lines (for introductions, see, e.g., [1–6]). Spectra show a mind-boggling variety of broad emission line profiles not only among different objects but also among different lines in the spectrum of the same object. Sulentic [7] carried out measurements of spectral shifts and asymmetries exhibited by the broad lines relative to the narrow ones, proposing an empirical classification scheme for the broad H $\beta$  Balmer line. Among the classes identified by Sulentic [7], two stand out: AR,R and AR,B, where AR means red-ward asymmetric, and the letter after the comma indicates either a shift of the line peak toward red or blue.

Fast forward more than 30 years, type-1 quasars are now being contextualized on the basis of the main sequence (MS) trends (e.g., [1,8,9]). Type-1 AGNs have been grouped into two main populations, Population A and B, defined on the basis of Balmer line widths (more specifically of H $\beta$ : FWHM H $\beta$   $\lesssim$  4000 km s<sup>-1</sup> for Population A; FWHM H $\beta$   $\gtrsim$  4000 km s<sup>-1</sup> for Population B [1,10] at low and moderate luminosity log  $L \lesssim 46$  (erg s<sup>-1</sup>)). The classification of the quasar population along MS has its main physical foundation on systematic differences in Eddington ratio [11]: Population A sources typically have  $L/L_{\text{Edd}} \gtrsim 0.2$ , with extreme Population A sources reaching  $L/L_{\text{Edd}} \gtrsim 1$  [12], values close to the expected theoretical limit for super-Eddington accretion rate [13–15]. Usually, Pop. B sources present lower values of the Eddington ratio when compared with the ones of Pop. A. The governing parameter of the MS itself appears to be an Eddington ratio convolved with the effect of orientation (e.g., [16,17]).<sup>1</sup>

Sources showing prominent  $H\beta$  red asymmetries (i.e., AR,R according to Sulentic [7]) are classified as belonging to Population B [10,11]. The red asymmetry itself can be considered as a defining feature of Population B sources, hinting at the presence of a “very broad component” (VBC) at the line base [18–23]. The physical properties of the region associated with VBC are largely undetermined (e.g., [24]) but the general consensus is that the region is located at the innermost radii of the broad line region (BLR), closest to the central continuum source. This inference follows from the deduction of a velocity field dominated by virial motions, at least for several population B sources [25,26]. The dynamical conditions of the “very broad line region” (VBLR) are the subject of current debate [27]. Two main alternatives have been proposed: infall and obscuration [28], or gravitational and transverse redshift [27,29–33]. Both mechanisms are, however, still consistent with a virial velocity field as the main broadening factor.

Gaseous outflows appear to be ubiquitous in type-1 AGN, although their traceability and their kinetic power varies greatly along the main sequence [34,35]. The signature of outflows in the optical and UV spectra is provided by the blueshift of emission lines with respect to the rest frame, under the assumption that the shift is due to a Doppler effect on the wavelength of lines emitted by gas moving toward us and that the receding side of the flow is mainly hidden from view (e.g., [36]). While there is unambiguous evidence of outflows from the emitting regions of quasars radiating at high Eddington ratios, the situation is by far less clear for Pop. B where the accretion rate is modest, as implied by a Eddington ratio  $\lesssim 0.2$ . High-resolution X-ray and ultraviolet (UV) observations of the prototypical Population B source NGC 5548 reveal a persistent ionized outflow traced by UV and X-ray absorption and emission lines [37]. However, the CIV emission line profile lacks strong evidence of such an outflow also because of the prominent red line wing merging with  $\text{HeII}\lambda 1640$  [38].

In this short note, we address the very specific issue of the origin of sources showing a blueshift at the peak of the  $H\beta$  emission line, e.g., of the AR,B classification. The focus is on the  $H\beta$  line because the line is a singlet, and its peak is isolated from other contaminants, offering a clear view of its broad and narrow components. The  $[\text{OIII}]\lambda\lambda 4959,5007$  lines recorded along with  $H\beta$  help assess the nature of the  $H\beta$  line profile. In addition, the narrow, high-ionization  $[\text{OIII}]\lambda 5007$  emission lines are known to be affected by outflows, as indicated by the frequent blueward asymmetries and even systematic shifts [39–43]. Section 2 presents the data used in this work, which comprise a set of composite spectra covering a wide range in luminosity and redshift, for which  $H\beta$  and  $[\text{OIII}]\lambda\lambda 4959,5007$  emissions have been covered with optical and IR spectroscopic observations. Details on how the spectral analysis was performed are shown in Section 3. The main results come from the profile comparison of  $H\beta$  and  $[\text{OIII}]\lambda 5007$  (Section 4) and are briefly analyzed in terms of the physical conditions of the line emitting gas, as well as of the dynamical parameters of the outflow (Section 5).

## 2. Data

The data analyzed in this paper refer to the most widely populated spectral type of Population B, B1, defined by FWHM  $H\beta$  in the range of 4000–8000  $\text{km s}^{-1}$  [44]. Median composite spectra covering the  $H\beta$  range were computed over spectral type B1 sources belonging to two samples of low-to-moderate redshift and luminosity [44,45], and one sample of intermediate  $z$  and high luminosity [46]. The [44] composites are based on the individual observations of Marziani et al. [47] that involved 97 B1 spectra. The [45] composites are SDSS spectra in the redshift range of 0.4–0.7, covering both  $\text{MgII}\lambda 2800$  and  $H\beta$ . The radio-quiet B1 composite was computed over 179 spectra, while CD and FR-II composites involved 16 and 23 spectra, respectively. The [46] B1 composite included 22 high-luminosity, Hamburg ESO (HE) quasars. Median composites were constructed from continuum-normalized (at 5100 Å) spectra, after a determination of the heliocentric redshift based on  $[\text{OII}]\lambda 3727$  or a narrow component of  $H\beta$ , two low-ionization narrow line that provide the best estimators of the systemic redshift of the host galaxy [48]. The accurate redshift correction allowed for the preservation of the spectral resolution of the individual

spectra. The [45] composites should, therefore, have a resolving power  $\lambda/\delta\lambda \sim 2000$ . The resolving power is only slightly lower for [44],  $\lambda/\delta\lambda \sim 1000$ . The HE ISAAC near-IR observations were all collected with a narrow slit (0.6 arcsec) that yielded  $\lambda/\delta\lambda \sim 1000$ , comparable to the spectra of the samples observed with optical spectrometers. The main physical properties associated with the composite spectra are summarized in Table 1, where the first column lists an identification code, and the following columns list the redshift range and the median values of bolometric luminosity, black hole mass  $M_{\text{BH}}$ , and the Eddington ratio  $L/L_{\text{Edd}}$ . In addition to the composite spectra, the spectra of two quasars of extreme luminosity at intermediate redshift (Deconto-Machado et al. 2022, in preparation) provide examples of two opposite cases: One where a prominent outflow signature is detected (Q0029+079), and one in which there is no obvious evidence of outflow (HE0001-2340). The last two lines of Table 1 consider composites for core-dominated (CD) and Fanaroff–Riley (FR) sources belonging to spectral type B1 from the [45] sample. These two composite were defined to address the somewhat controversial issue of the mild-ionized outflow presence among radio-loud, jetted AGN.<sup>2</sup> The data of Table 1 confirm that the empirical selection of spectral type B1 corresponds to the selection of modest  $L/L_{\text{Edd}}$  radiators. At the higher redshift and luminosity,  $L/L_{\text{Edd}}$  appears somewhat higher ( $L/L_{\text{Edd}} \approx 0.3$ ) because of the preferential selection of higher  $L/L_{\text{Edd}}$  for a fixed black hole mass in flux limited surveys [51].

**Table 1.** Physical parameters.

Spectrum	$z$	$\log L$ ( $\text{erg s}^{-1}$ )	$\log M_{\text{BH}}^a$ ( $M_{\odot}$ )	$\log L/L_{\text{Edd}}$
Composite spectra				
B1 [44]	0–0.7	45.63 <sup>b</sup>	8.52	−1.07
B1 [45]	0.4–0.7	46.31 <sup>b</sup>	9.19	−1.06
B1 [46]	0.9–2.6	47.29 <sup>c</sup>	9.63	−0.51
Individual, high- $L$ quasars				
HE0001–2340	2.2651	47.09 <sup>c</sup>	9.78	−0.86
Q0029+079	3.2798	47.43 <sup>c</sup>	9.95	−0.70
Composite spectra, jetted				
B1 [45] CD	0.4–0.7	46.51 <sup>b</sup>	9.39	−1.05
B1 [45] FR II	0.4–0.7	46.62 <sup>b</sup>	9.44	−1.00

<sup>a</sup>: Black hole mass computed from the  $H\beta$  scaling law provided by Vestergaard and Peterson [52], using the  $H\beta$  full profile FWHM. Applying the average correction suggested for spectral type B1 would lower the mass by a factor 0.64 and increase the  $L/L_{\text{Edd}}$  ratio by the inverse of this factor. <sup>b</sup> Bolometric correction assumed a factor 10; <sup>c</sup> Bolometric correction assumed a factor 4, as appropriate for very high luminosity sources following Netzer [53].

### 3. Analysis

The non-linear multicomponent fits were performed using the SPECFIT routine from IRAF [54]. This routine allows a simultaneous minimum- $\chi^2$  fit of the continuum approximated by a power law and the spectral line components yielding FWHM, peak wavelength, and intensity of all line components. In the optical range, we fit the  $H\beta$  profile as well as the [OIII] $\lambda\lambda 4959, 5007$  emission lines and the FeII multiplets accounted for by a scaled and broadened template [55]. The details of multi-component analysis has been provided in several previous papers (e.g., [56]) and will not be repeated here. Suffice to say that the broad profiles of Pop. B sources can be successfully modeled with two Gaussians: (1) one narrower, unshifted or slightly shifted to the red; and (2) one broader, with FWHM  $\sim 10,000 \text{ km s}^{-1}$ , and shifted by few thousands  $\text{km s}^{-1}$  to the red [57]. This model accounts for the AR,R profile type. In addition to the model decomposition, we measured

several parameters on the full broad profile [58]. The definitions of the centroids and of the asymmetry index  $A.I.$  are reported below for convenience:

$$c\left(\frac{i}{4}\right) = \frac{v_{r,B}\left(\frac{i}{4}\right) + v_{r,R}\left(\frac{i}{4}\right)}{2}, \quad i = 1, 2, 3; \quad \frac{i}{4} = 0.9, \quad (1)$$

where the radial velocities are measured with respect to the rest frame at fractional intensities  $\frac{i}{4}$  for each value of the index  $i$  on the blue and red side of the line with respect to the rest frame.

$$A.I.\left(\frac{1}{4}\right) = \frac{v_{r,B}\left(\frac{1}{4}\right) + v_{r,R}\left(\frac{1}{4}\right) - 2v_{r,P}}{v_{r,R}\left(\frac{1}{4}\right) - v_{r,B}\left(\frac{1}{4}\right)}. \quad (2)$$

Note that the  $A.I.$ , unlike the centroids, is defined as a shift with respect to the line peak radial velocity  $v_{r,P}$  ( $v_{r,P}$  is measured with respect to rest frame; a suitable proxy is provided by  $c(0.9)$ ).

## 4. Results

### 4.1. Broad H $\beta$

Figure 1 shows the continuum-subtracted spectra and their models for the [44–46] composite spectra (top, middle and bottom panel, respectively). The measurements of the broad H $\beta$  line parameters are reported in Table 2. For each spectrum, Table 2 lists the normalized flux  $F$  of the H $\beta$  full broad profile (H $\beta_{BC}$  + H $\beta_{VBC}$  + H $\beta_{BLUE}$ ), its equivalent width  $W$  H $\beta$  in Å, and the normalized fluxes of H $\beta_{BC}$  and H $\beta_{VBC}$  separately. The following columns report several parameters for the H $\beta$  blue-shifted excess with respect to the standard Population B decomposition involving only H $\beta_{BC}$  and H $\beta_{VBC}$ : normalized flux, equivalent width, peak shift, FWHM, and skew. The last columns yield the normalized flux and the equivalent width of the FeII $\lambda$ 4570 emission blend, as defined by Boroson and Green [55]. The equivalent width values correspond roughly to the normalized flux so that they are reported only for the main features. The normalized fluxes can be approximately converted into luminosities by multiplying them by the luminosity values reported in Table 1 divided by the bolometric correction and by 5100, i.e., by the wavelength in Å at which the continuum was normalized. Table 3 reports FWHM,  $A.I.$ , and centroids as defined in Section 3 for the *broad* H $\beta$  profile (H $\beta_{BC}$  + H $\beta_{VBC}$  + H $\beta_{BLUE}$  i.e., without considering the narrow (H $\beta_{NC}$ ) and semi-broad (H $\beta_{SBC}$ ) components associated with narrow-line region emission). Only at the highest  $L$  blueshifted emission with a broad profile (H $\beta_{BLUE}$ ) is detected in the H $\beta$  profile: In this case, the H $\beta_{BLUE}$  contribution is  $\lesssim 5\%$  of the total line luminosity for the [46] composite and reaches about 1/3 of the total line luminosity in the admittedly extreme Q0029 case. In no case, however, was H $\beta_{BLUE}$  able to create a significant shift to the blue close to the line base: red asymmetry dominates and even the Q0029 H $\beta$  broad profile is “symmetrized” toward the line base, with a centroid at  $\frac{1}{4}$  peak intensity close to 0 km s $^{-1}$ .

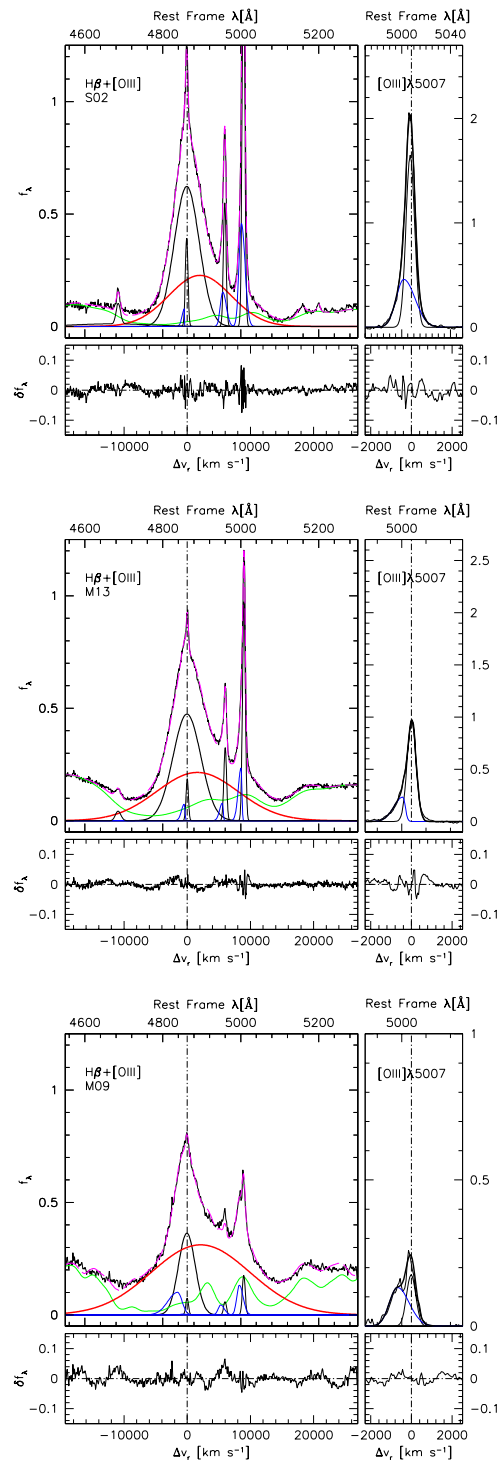


**Figure 1.** Analysis of the  $H\beta + [OIII]\lambda\lambda 4959,5007$  region for [44] (top), [45] (middle), and [46] (bottom) B1 composite spectra. Continuum subtracted spectra are shown in the rest frame, over the range 4550–5300 Å (left panel), with an expansion around  $[OIII]\lambda 5007$  (right panels). Thin solid lines: continuum-subtracted spectrum; dashed magenta line: model spectrum; thick black line:  $H\beta$  broad component; red thick line,  $H\beta$  very broad component; thin smooth black lines: narrow components of  $H\beta$  and  $[OIII]\lambda 5007$ ; blue lines: blue shifted components. Green lines trace the scaled and broadened FeII emission template. The lower panel show the observed minus model residuals in radial velocity scale.

**Table 2.** Broadline properties measurements.

Spectrum	H $\beta$		H $\beta_{BC}$	H $\beta_{VBC}$	F	H $\beta_{BLUE}$		Skew <sup>c</sup>	FeII $\lambda$ 4570	
	F	W <sup>a</sup>	F	F		Shift <sup>b</sup>	FWHM <sup>b</sup>		F	W
Composite spectra										
B1 [44]	95.3	86.7	49.8	45.4	...	...	...	...	18.1	14.6
B1 [45]	122.3	126.5	52.5	69.8	...	...	...	...	47.8	43.0
B1 [46]	123.3	129.1	19.6	99.1	4.6	−1535	3611	0.5	39.2	34.1
Individual, high- <i>L</i> quasars										
HE0001	99.3	95.1	26.7	72.7	...	...	...	...	20.6	16.3
Q0029	69.8	66.4	13.9	32.2	23.7	−2097	4711	1.2	25.8	21.4
Composite spectra, jetted										
B1 [45] CD	113.8	118.5	42.9	70.9	...	...	...	...	35.6	32.7
B1 [45] FRII	129.8	131.1	57.5	72.3	...	...	...	...	24.6	21.9

<sup>a</sup>: In units of Å; <sup>b</sup>: in units of km s<sup>−1</sup>. <sup>c</sup> skew as reported by the SPECFIT routine; it is equal to the conventional definition of skew [59] + 1.

**Table 3.** H $\beta$  profile properties measurements.

Spectrum	FWHM <sup>a</sup>	AI	c(1/4) <sup>a</sup>	c(1/2) <sup>a</sup>	c(3/4) <sup>a</sup>	c(0.9) <sup>a</sup>
Composite spectra						
B1 [44]	5560 ± 170	0.12 ± 0.03	680 ± 230	250 ± 80	160 ± 70	130 ± 50
B1 [45]	6540 ± 210	0.12 ± 0.06	740 ± 340	150 ± 110	50 ± 90	40 ± 60
B1 [46]	6010 ± 450	0.28 ± 0.06	2120 ± 490	−50 ± 220	−230 ± 70	−270 ± 50
Individual, high- <i>L</i> quasars						
HE0001	6510 ± 690	0.29 ± 0.09	2700 ± 560	1310 ± 340	900 ± 170	830 ± 110
Q0029	6200 ± 380	0.18 ± 0.10	430 ± 500	−380 ± 190	−500 ± 160	−500 ± 110
Composite spectra, jetted						
B1 [45] CD	6880 ± 240	0.23 ± 0.06	1520 ± 380	270 ± 120	70 ± 90	20 ± 60
B1 [45] FRII	6790 ± 220	0.10 ± 0.06	820 ± 330	320 ± 110	240 ± 90	230 ± 60

<sup>a</sup> In units of km s<sup>−1</sup>.

#### 4.2. [OIII] $\lambda$ 5007 and H $\beta$ Narrow-Line Emission

Table 4 summarizes the measurements of the components associated with the narrow-line region (NLR) emission, i.e., narrow and semi-broad components of H $\beta$  and [OIII] $\lambda$ 5007 (H $\beta_{NC}$ , [OIII] $\lambda$ 5007<sub>NC</sub>, and H $\beta_{SBC}$  and [OIII] $\lambda$ 5007<sub>SBC</sub>), for which normalized flux, equivalent width, shift, and FWHM are reported. The skew parameter is reported only for semi-broad components, as the narrow components are assumed to be symmetric Gaussian, within a few tens km s<sup>−1</sup> from the rest frame [48].

The [44] composite shows a broad + narrow component profile that is very well represented by three Gaussians: the symmetric unshifted H $\beta_{NC}$ , unshifted H $\beta_{BC}$  and the H $\beta_{VBC}$  with a significant shift to red. A small blue-shifted excess appears at the interface between H $\beta_{NC}$  and H $\beta_{BC}$  and has been modeled by an additional Gaussian. Its intensity is so low that a very good fit with no significant worsening in the  $\chi^2$  can be achieved also without it. Most notably, the [OIII] $\lambda$ 5007 profile (enlarged in the right panel) is also fairly symmetric: A small centroid blueshift  $\sim -50$  km s<sup>−1</sup> is detected only at  $\frac{1}{4}$  peak intensity (Table 5, where the [OIII] $\lambda$ 5007 full profile parameters are reported as in Table 3 for H $\beta$ ). The relatively large shift reported for [OIII] $\lambda$ 5007<sub>SBC</sub> is compensated by a red-ward skew (Figure 1, right panel on top row). In this case, the decomposition [OIII] $\lambda$ 5007<sub>NC</sub>-[OIII] $\lambda$ 5007<sub>SBC</sub> is especially uncertain, and a more reliable measurement is provided by the centroid.

**Table 4.** Narrow line measurements.

Spectrum	$H\beta_{\text{NC}}$			$H\beta_{\text{SBC}}$			$[\text{OIII}]\lambda 5007_{\text{NC}}$			$[\text{OIII}]\lambda 5007_{\text{SBC}}$								
	F	W <sup>a</sup>	Shift <sup>b</sup>	FWHM <sup>b</sup>	F	W <sup>a</sup>	Shift <sup>b</sup>	FWHM <sup>b</sup>	Skew <sup>c</sup>	F	W <sup>a</sup>	Shift <sup>b</sup>	FWHM <sup>b</sup>	F	W <sup>a</sup>	Shift <sup>b</sup>	FWHM <sup>b</sup>	Skew <sup>c</sup>
Composite spectra																		
B1 [44]	3.33	3.00	−9	492	0.59	0.53	−349	881	...	14.6	14.0	12	499	8.86	8.45	−307	881	1.47
B1 [45]	1.45	1.45	−8	450	0.83	0.85	−480	1054	0.26	8.9	9.7	11	513	2.76	3.00	−417	1054	0.26
B1 [46]	0.65	0.70	−25	508	0.06	0.07	−752	932	1.46	1.6	1.8	−15	528	2.68	2.97	−688	932	1.46
Individual, high- <i>L</i> quasars																		
HE0001	0.11	0.10	−25	2202	1.05	0.99	−133	1301	0.41	2.6	2.7	239	592	4.39	4.43	−69	1301	0.41
Q0029	1.00	0.95	−6	1181	0.00	0.00	...	...	...	4.9	4.9	−728	1181	3.36	3.30	−2051	1340	1.12
Composite spectra, jetted																		
B1 [45] CD	1.92	1.96	−25	662	0.00	0.00	...	...	...	6.8	7.4	20	497	5.17	5.62	39	1439	0.10
B1 [45] FR II	0.94	0.98	−25	300	0.00	0.00	...	...	...	13.5	13.0	11	360	7.65	8.11	−279	585	2.12

<sup>a</sup>: In units of Å; <sup>b</sup>: in units of km s<sup>−1</sup>. <sup>c</sup> skew as reported by the SPECFIT routine; it is equal to the conventional definition of skew [59] + 1.

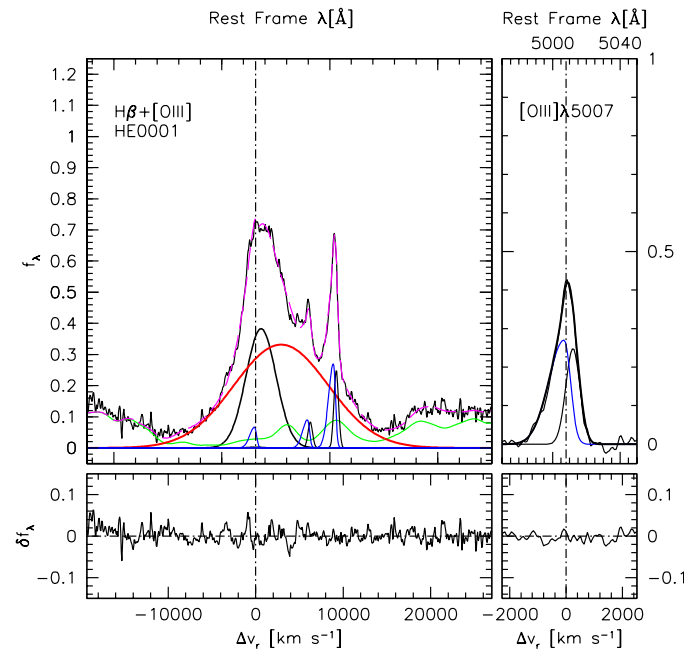
**Table 5.** [OIII] $\lambda$ 5007 profile measurement.

Spectrum	FWHM <sup>a</sup>	AI	c(1/4) <sup>a</sup>	c(1/2) <sup>a</sup>	c(3/4) <sup>a</sup>	c(0.9) <sup>a</sup>
Composite spectra						
B1S02	580 $\pm$ 30	-0.10 $\pm$ 0.08	-40 $\pm$ 40	-10 $\pm$ 20	0 $\pm$ 20	0 $\pm$ 10
B1M13	560 $\pm$ 40	-0.23 $\pm$ 0.11	-80 $\pm$ 50	-20 $\pm$ 20	10 $\pm$ 10	30 $\pm$ 10
B1M09	1100 $\pm$ 120	-0.43 $\pm$ 0.05	-380 $\pm$ 40	-280 $\pm$ 60	-60 $\pm$ 20	-40 $\pm$ 10
Individual, high- <i>L</i> quasars						
HE0001	900 $\pm$ 70	-0.26 $\pm$ 0.07	-100 $\pm$ 40	0 $\pm$ 30	70 $\pm$ 30	80 $\pm$ 10
Q0029	2120 $\pm$ 140	-0.37 $\pm$ 0.04	-1360 $\pm$ 60	-1240 $\pm$ 70	-860 $\pm$ 50	-830 $\pm$ 30
Composite spectra, jetted						
B1M13CD	490 $\pm$ 40	-0.18 $\pm$ 0.12	-90 $\pm$ 50	-70 $\pm$ 20	-10 $\pm$ 20	-10 $\pm$ 10
B1M13FRII	440 $\pm$ 30	-0.10 $\pm$ 0.09	-20 $\pm$ 30	10 $\pm$ 10	10 $\pm$ 10	10 $\pm$ 10

<sup>a</sup>: In units of km s<sup>-1</sup>.

The [45] composite spectrum appears as a “goiter” at the top of the H $\beta$ <sub>BC</sub> broad profile. The [OIII] $\lambda$ 5007 profile is also fairly asymmetric, and it can be modeled by a narrower, almost unshifted component and a skewed Gaussian displaced to the blue by  $\approx -500$  km s<sup>-1</sup>. The top of the H $\beta$  profile is well fit by assuming two components with the same shift, width, and asymmetry of the model components’ [OIII] $\lambda$ 5007 line. The consistency between the model of H $\beta$ <sub>SBC</sub> and [OIII] $\lambda$ 5007<sub>SBC</sub> provides evidence that the H $\beta$  blueshifted, and the skewed component is associated with a NLR outflow. The [46] composite can be equally modeled with the same skewed and blueshifted component for H $\beta$  and [OIII] $\lambda$ 5007. However, this model would require an implausibly strong [OIII] $\lambda$ 4959,5007 emission. The fit shown in the bottom panel of Figure 1 assumes a broader component for H $\beta$  emission.

At very high luminosity (Figure 2), a prominent outflow is apparently absent in one Pop. B H $\beta$  profile (HE0001) but very prominent in another (Q0029). If the classification of Q0029 as a Population B source is correct, the model of the blue “goiter” at the side of the H $\beta$  profile implies a strong contribution of blueshifted emission with a broad profile. The [OIII] $\lambda$ 5007 profiles are also different: the equivalent width *W* is higher and the shift is lower in the case of HE0001, where no significant H $\beta$  outflow is detected. By all means, the properties of Q0029 appear more extreme. We predict that this source will show extreme CIV blueshift, with an amplitude of several thousands km s<sup>-1</sup>.

**Figure 2.** Cont.

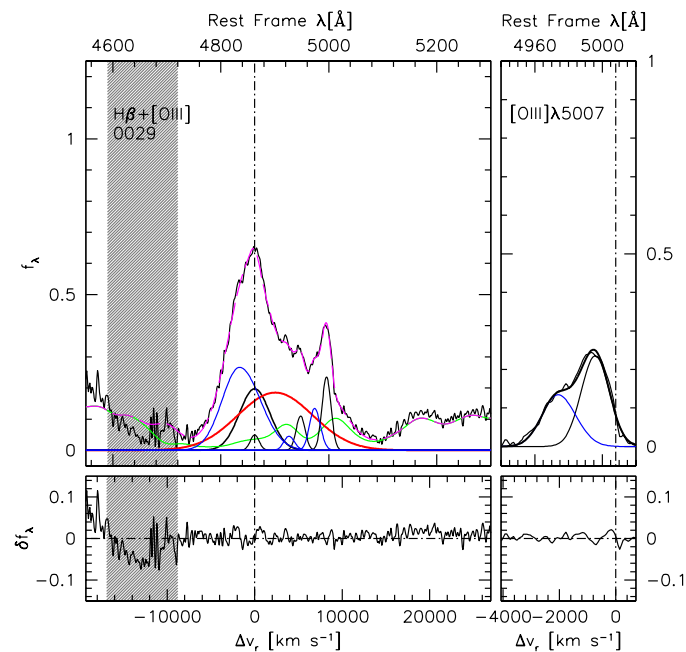


**Figure 2.** Analysis of the  $H\beta + [OIII]\lambda\lambda 4959,5007$  region for two high-luminosity, high- $z$  quasars belonging to the B1 spectral type. The top one, HE0001-234, shows no appreciable evidence of blueshift, while the bottom one (HB89) 0029+073 requires a stronger blue shifted excess for  $[OIII]\lambda\lambda 4959,5007$  and an even stronger and broader one to fit  $H\beta$ . Color coding of the components is the same as in the previous Figure. The shaded area identifies a spectral region affected by atmospheric absorptions

The  $[OIII]\lambda 5007$  shift and the A.I. become more negative, and the equivalent width decreases with increasing luminosity. This is a pure luminosity effect that proceeds in the same sense of the effect of an increasing Eddington ratio in sample covering the full span of  $L/L_{Edd} \sim 10^{-2} - 1$ , and it can be interpreted as a result of NLR evolution with redshift [35].

#### 4.3. Jetted Sources

The CD and FR-II composites from the [45] sample (Figure 3) show that the  $[OIII]\lambda 5007$  blueshifted and skewed component is not detected in  $H\beta$ , implying that the intensity ratio is  $[OIII]\lambda 5007/H\beta \gg 1$  for this component. In addition, the  $[OIII]\lambda 5007$  profile for the FR-II composite spectrum is much more symmetric than that of the CD composite, for which its A.I. and centroid shifts are more consistent with the RQ composite of the same sample. This systematic difference may arise because of the different viewing angles expected for CD (seen almost pole on) and FR-II sources (seen at a viewing angle  $\approx 40-60$  [60]).

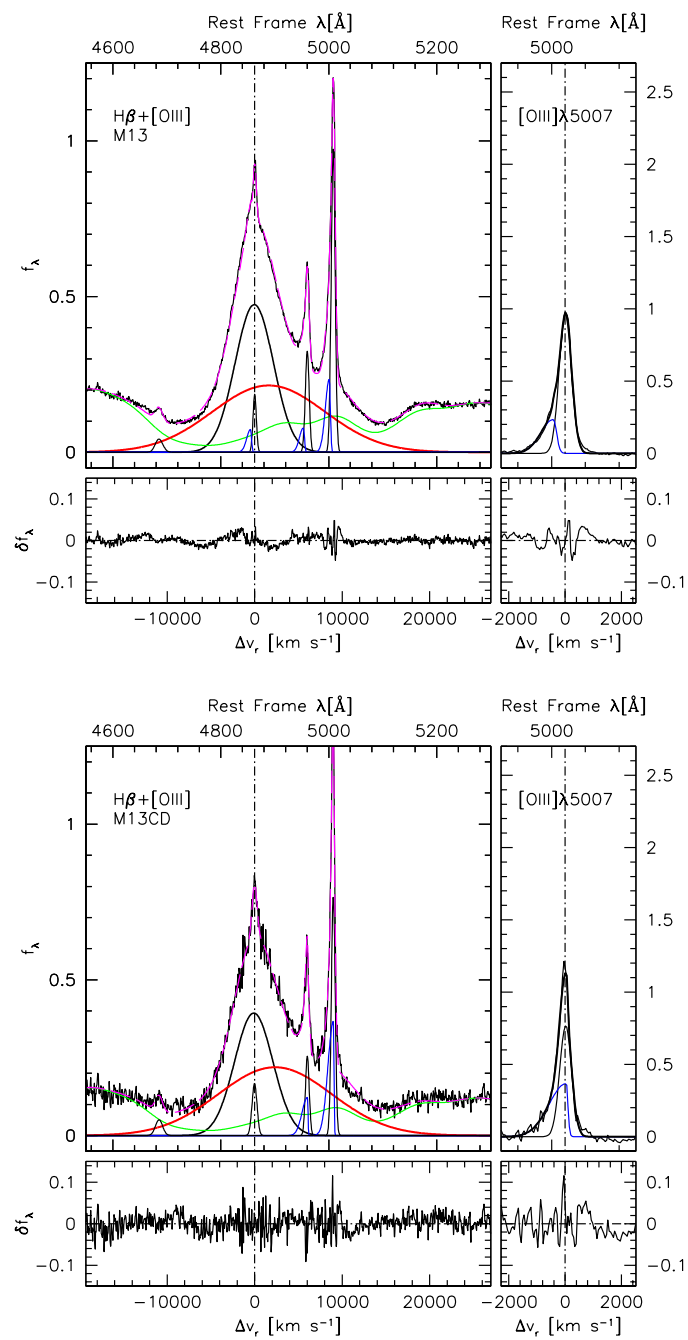
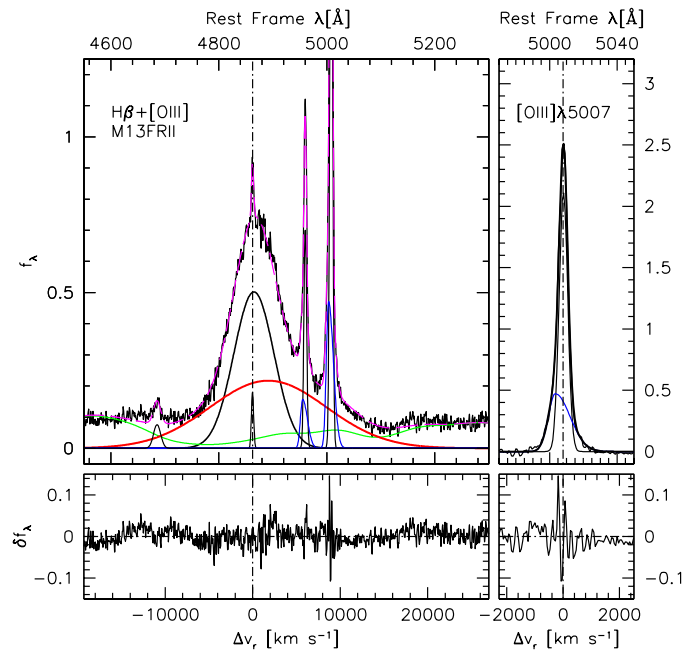


Figure 3. Cont.



**Figure 3.** Analysis of the  $H\beta + [OIII]\lambda\lambda 4959,5007$  region for the RQ composite spectrum of Marziani et al. [45] (**top**), and for the CD and FR-II composite spectra (**middle** and **bottom**, respectively). Color coding of the components is the same as in the previous Figures.

## 5. Discussion

The analysis performed above has been focused on sources radiating at relatively modest  $L/L_{\text{Edd}}$  (Population B) but covering a wide range of redshifts ( $0 \lesssim z \lesssim 3$ ) and luminosities. Significant outflow features have been detected in NLR, as traced by  $H\beta$  and  $[OIII]\lambda\lambda 4959,5007$  blue shifted components. At high luminosity, significant blueshifts are found not only in the  $[OIII]\lambda\lambda 4959,5007$  lines but also with a broader profile, hinting at an association with BLR emission.

### 5.1. How Important Is the Outflow Component?

The present analysis relies on the important assumption that the Population B profile at  $H\beta$  low- $z$  and luminosity is not significantly affected by any outflowing gas. Reverberation mapping campaigns in the early 2000s provided evidence that the main broadening mechanism is indeed provided by a virial velocity field of gas orbiting around a point-like mass. More recent works point toward a more complex situation ([61–63] Bao et al., 2022, in preparation), although the main inference from velocity-resolved reverberation mapping studies for the sources with the red  $H\beta$  asymmetry is that the velocity field is predominantly virial, with the frequent detection of infall motions. The detection of infall is based on the shorter time delay of the red wing and not on the response of the line core.

### 5.2. Identifying an Outflow Component

The  $H\beta$  profile of Population B presents a clear inflection between  $H\beta_{\text{BC}}$  and  $H\beta_{\text{NC}}$  that can be explained on the basis of the expected radial emissivity of  $H\beta$  [64]. The identification of an outflow component may be achieved by considering the following options:

- No significant centroid blueshift in the broad profile of  $H\beta$  and symmetric appearance at the interface between  $H\beta_{\text{NC}}$  and  $H\beta_{\text{BC}}$ , with the peak of the broad profile showing no shift or a slight redshift: no evidence of outflow.
- No significant centroid blueshift in the broad profile of  $H\beta$  and “goiter” appearance at the interface between  $H\beta_{\text{NC}}$  and  $H\beta_{\text{BC}}$ : If the  $[OIII]\lambda 5007$  line shows a significant blueward asymmetry and a model of the  $[OIII]\lambda 5007$  line profile with a core and

semi-broad component is applicable to the  $H\beta$  profile, then it is likely that the outflow is mainly associated with NLR emission.

- Even modest centroid blueshift in the broad profile of  $H\beta$  at fractional intensity  $\frac{3}{4}$  or 0.9, the outflow might involve BLR emission. In this case,  $H\beta_{\text{BLUE}}$  corresponds to the prominent blueshifted emission of the CIV line observed at high luminosity [56]. The detection of  $H\beta_{\text{BLUE}}$  is made more difficult by the CIV/ $H\beta$  ratio expected to be  $\gg 1$ .

### 5.3. Location and Physical Nature of the Outflow

Even in case of modest accretion rate, the outflow can be radiatively driven [65]. The ratio between the radiation and gravitation force can be written as  $a_{\text{rad}}/a_{\text{grav}} \approx 7.2 L/L_{\text{Edd}} N_{\text{c},23}^{-1}$  where  $N_{\text{c},23}$  is the Hydrogen column density in units of  $10^{23} \text{ cm}^{-2}$  (e.g., [66]). For  $L/L_{\text{Edd}} \sim 0.1$ , the gas of moderate common density  $N_{\text{c},23} \sim 0.1$  could be accelerated to  $a_{\text{rad}}/a_{\text{grav}} \sim 10$  (c.f. Equation (6) of Netzer and Marziani [65]) [67]. The first underlying assumption is that all of the photon's momentum in the ionizing continuum is transferred to the line-emitting gas. The second assumption is that the gas is optically thick relative to the ionizing continuum, and this condition is more easily verified if the ionization parameter is low, implying that the low column density gas located farther out from the AGN continuum source might be preferentially accelerated. This might explain why we see a signature due to a semi-broad component in  $H\beta$ ,  $H\beta_{\text{SBC}}$ , which is in turn associated with the [OIII] $\lambda 5007$  semi-broad component, likely at the inner edge of NLR, and it may be the main signature of outflow in low  $L/L_{\text{Edd}}$  sources.

Regarding BLR, at low luminosity, there is no signature of outflow, if our interpretation of the profile is correct. For Population B sources, however, the observed spectrum can be explained by the locally optimized cloud (LOC) scheme, in which a range of ionization parameters, density, and column density is assumed, and the emerging spectrum is set by the parameters at which lines are emitted most efficiently [68,69]. This is to say that there might be always gas as "light" as needed for an outflow; however, the outflow may not produce a significant signature in the emission line spectrum. A powerful outflow at a modest Eddington ratio may become possible only at high luminosity (e.g., [70–72]), as predicted from wind theory and confirmed by observations [56,73–75].

### 5.4. The Fate of the Outflowing Gas: No Feedback Effects at Low $L$

The mass outflow rate at a distance  $r$  can be written as follows if the flow is confined to a solid angle of  $\Omega$  of volume  $\frac{4}{3}\pi r^3 \frac{\Omega}{4\pi}$ :  $\dot{M}_{\text{ion}} = \rho \Omega r^2 v_o = \frac{M_{\text{ion}}}{V} \Omega r^2 v_o \propto L v_o r^{-1}$  [76]; it implies  $\dot{M}_{\text{ion}} \sim 30 L_{44} v_{o,1000} r_{1\text{kpc}}^{-1} \left(\frac{Z}{5Z_{\odot}}\right)^{-1} n_3^{-1}$ , where the mass of ionized gas can be directly estimated from the line luminosity:  $M_{\text{ion}} \sim 1 \cdot 10^7 L_{44} \left(\frac{Z}{5Z_{\odot}}\right)^{-1} n_3^{-1}$ .<sup>3</sup> The low-luminosity cases [44,45] imply that the outflow velocity is  $v_{o,1000} \sim 1$  from the peak shift of [OIII] $\lambda 5007_{\text{SBC}}$ , and the [OIII] $\lambda 5007_{\text{SBC}}$  luminosity is  $\log L_{[\text{OIII}]}$   $\sim 42$ . Assuming  $Z \approx 1Z_{\odot}$  as appropriate for Population B sources [27],  $M_{\text{ion}} \sim 5 \cdot 10^5 n_3^{-1}$  and  $\dot{M}_{\text{ion}} \sim 0.15 r_{1\text{kpc}}^{-1} n_3^{-1}$ . By the same token, the thrust and kinetic power can be written as  $\dot{M}v \sim 1.9 \cdot 10^{35} L_{44} v_{o,1000}^2 r_{1\text{kpc}}^{-1} \left(\frac{Z}{5Z_{\odot}}\right)^{-1} n_3^{-1}$  and  $\dot{\epsilon} \sim 10^{43} L_{44} v_{o,1000}^3 r_{1\text{kpc}}^{-1} \left(\frac{Z}{5Z_{\odot}}\right)^{-1} n_3^{-1}$ , which become  $\dot{M}v \sim 1 \cdot 10^{34} r_{1\text{kpc}}^{-1} n_3^{-1}$  and  $\dot{\epsilon} \sim 5 \cdot 10^{41} r_{1\text{kpc}}^{-1} n_3^{-1}$ . Even assuming that we are observing a flow at  $r \sim 10 \text{ pc}$ , the kinetic power is  $\dot{\epsilon} \lesssim 10^{44} \text{ erg s}^{-1}$ , a factor  $\approx 100$  below the bolometric luminosity and  $\approx 1000$  the Eddington luminosity of the [45] case. The emitting gas might be beyond or at the limit of the black hole sphere of influence given by  $r \approx GM/\sigma_{\star}^2 \approx 8 \cdot 10^{19} M_{9,\odot}/\sigma_{\star,400}^2 \text{ cm}$ , where  $\sigma_{\star}$  is the velocity dispersion associated with the bulge of the host galaxy in units of  $400 \text{ km s}^{-1}$ . At this radius, the escape velocity is expected to be  $v_{\text{esc}} \sim 500 \text{ km s}^{-1}$  for a  $10^9 M_{\odot}$  black hole. It is, therefore, doubtful whether the outflowing gas might be even able to escape from the sphere of influence of the black hole. Even less likely, the outflowing gas might "wreak havoc" galaxy-wide in the bulge and the disk of

the host due to the small amount of gas masses involved in the outflow, and due to the escape velocity that can be as high as  $v_{\text{esc}} \gtrsim 1000 \text{ km s}^{-1}$  in the inner regions of a massive spheroid or in a giant spiral such as the Milky Way [77].

The scenario might radically change at high luminosity: considering the [46] composite, the velocity of  $[\text{OIII}]\lambda 5007_{\text{SBC}}$  is higher by a factor  $\approx 2$ , and the line luminosity is higher by a factor  $\sim 10$ , implying a 20-, 40-, and  $\sim 100$ -fold increase over the [45] case in mass flow, thrust, and kinetic power, respectively. In the [46] case, the kinetic power would be comparable to the Eddington luminosity. An even more powerful outflow is expected for Q0029.

## 6. Summary and Conclusions

The analysis of outflow signatures carried out in the present paper has been focused on three samples of type-1 AGN covering a wide range of luminosity.

The detection of different kinematic components in single epoch profiles is a complicated issue. The apertures and slit widths used in ground-based observation add up the emission from the AGN continuum, BLR, NLR, and host galaxy, which are associated with widely different spatial scales. The case of Population B sources of spectral type B1 is particularly well-suited to analyze the presence of an outflow component in the Balmer  $H\beta$  line for sources that are radiating at modest Eddington ratios.

Generally speaking, the detection of significant systematic blueshifts in the centroid measurements can be taken as a signature of outflow. If the blueshift/blue asymmetry is confined at the top of the  $H\beta$  line and the  $H\beta$  narrow emission can be modeled as  $[\text{OIII}]\lambda 5007$  assuming a semi-broad and a narrow component with a similar parameter, then the evidence of the outflow (the “goiter” in the line profile) remains confined to the NLR. However, if the  $H\beta$  centroid at  $\frac{3}{4}$  or at lower fractional intensity is also blue shifted, it is likely that a BLR outflow is being detected. Low column density gas can be driven into an outflow by radiation forces. Blueshifts in the line core can be, therefore, straightforwardly interpreted by an outflow component, without invoking binary BLR, in turn pointing toward sub-parsec binary black holes. Other spectral types along the MS have been identified as frequently involving binary black hole candidates [78,79].

The estimates of mass flow, thrust, and kinetic power are highly uncertain because of the lack of spatially resolved data. This situation might be changing soon with the development of integral-field spectrographs. Nonetheless, even when maximizing the coarse estimates reported above, it is unlikely that the thrust and the kinetic power (only  $\sim 10^{-2}$  the Eddington luminosity as derived for the [44,45] samples) might have a strong impact on the host galaxy’s evolution and not to mention the possibility of driving the black hole mass—bulge correlation (e.g., and references therein [80]). Even if the  $[\text{OIII}]\lambda 5007$  samples only emission from mildly ionized gas and the mass flow might be dominated by the higher-ionization gas, for low luminosity AGNs such as the prototypical Population B Seyfert-1 NGC 5548, kinetic luminosity remains a very small fraction of the Eddington luminosity [37,81]. The situation is expected to change at the “cosmic noon” at redshifts in the range of 1–2, when the most luminous quasars are observed, and of which the [46] composite provides a representative spectrum.

**Author Contributions:** P.M. wrote most of the paper; A.D.-M. contributed to the analysis of spectra. A.D.-M. and A.D.O. Both contributed with suggestions and critical reading. All authors have read and agreed to the published version of the manuscript.

**Funding:** Funding for the Sloan Digital Sky Survey has been provided by the Alfred P. Sloan Foundation and the U.S. Department of Energy Office of Science. The SDSS web site is <http://www.sdss.org>. (accessed on 14 February 2022). SDSS-III is managed by the Astrophysical Research Consortium for the Participating Institutions of the SDSS-III Collaboration including the University of Arizona, the Brazilian Participation Group, Brookhaven National Laboratory, Carnegie Mellon University, University of Florida, the French Participation Group, the German Participation Group, Harvard University, the Instituto de Astrofísica de Canarias, the Michigan State/Notre Dame/JINA Participation Group, Johns Hopkins University, Lawrence Berkeley National Laboratory, Max Planck Institute

for Astrophysics, Max Planck Institute for Extraterrestrial Physics, New Mexico State University, University of Portsmouth, Princeton University, the Spanish Participation Group, University of Tokyo, University of Utah, Vanderbilt University, University of Virginia, University of Washington, and Yale University.

**Institutional Review Board Statement:** Not applicable.

**Informed Consent Statement:** Not applicable.

**Data Availability Statement:** Data could be made t available upon request.

**Acknowledgments:** A.D.M. and A.D.O. acknowledge financial support from the State Agency for Research of the Spanish MCIU through the project PID2019-106027GB-C41 and the “Center of Excellence Severo Ochoa” award to the Instituto de Astrofísica de Andalucía (SEV-2017-0709). A.D.M. acknowledges the support of the INPhINIT fellowship from the “la Caixa” Foundation (ID 100010434). The fellowship code is LCF/BQ/DI19/11730018.

**Conflicts of Interest:** The authors declare no conflict of interest.

### Abbreviations

The following abbreviations are used in this manuscript:

AGN	Active Galactic Nucleus/i;
BLR	Broad Line Region;
BC	Broad Component;
CD	Core Dominated;
FR-II	Fanaroff-Riley II;
FWHM	Full Width Half-Maximum;
HE	Hamburg-ESO;
ISAAC	Infrared Spectrometer And Array Camera;
IR	Infrared;
LOC	Locally Optimized Cloud;
MDPI	Multidisciplinary Digital Publishing Institute;
MS	Main Sequence;
NC	Narrow Component;
NGC	New General Catalogue;
NLR	Narrow Line Region;
RL	Radio loud;
RQ	Radio quiet;
SBC	Semi-Broad Component;
SDSS	Sloan Digital Sky Survey;
UV	Ultra-violet;
VBC	Very Broad Component;
VBLR	Very Broad Line Region.

### Notes

- <sup>1</sup> In flux limited samples, Pop. A and B may have similar luminosity distributions. If this is the case, Pop. B sources are expected to host more massive black holes, considering the systematic differences in the Eddington ratio.
- <sup>2</sup> We consider the attribute “radio-loud” as a synonym of relativistically jetted [49,50].
- <sup>3</sup> Note that the filling factor is not appearing explicitly because, by using line luminosity, we already are considering the volume of the line-emitting gas. The fraction of volume that is actually occupied by the line emitting gas then depends on its density.

### References

1. Sulentic, J.W.; Marziani, P.; Dultzin-Hacyan, D. Phenomenology of Broad Emission Lines in Active Galactic Nuclei. *Annu. Rev. Astron. Astrophys.* **2000**, *38*, 521–571. [[CrossRef](#)]
2. Osterbrock, D.E.; Mathews, W.G. Emission-line regions of active galaxies and QSOs. *Annu. Rev. Astron. Astrophys.* **1986**, *24*, 171–203. [[CrossRef](#)]
3. Netzer, H. AGN emission lines. In *Active Galactic Nuclei*; Blandford, R.D., Netzer, H., Woltjer, L., Courvoisier, T.J.-L., Mayor, M., Ed.; Springer: Berlin/Heidelberg, Germany, 1990; pp. 57–160.
4. Peterson, B.M. *An Introduction to Active Galactic Nuclei*; Cambridge University Press: Cambridge, UK, 1997.

5. Osterbrock, D.E.; Ferland, G.J. *Astrophysics of Gaseous Nebulae and Active Galactic Nuclei*; University Science Books: Mill Valley, CA, USA, 2006.
6. Marziani, P.; Dultzin-Hacyan, D.; Sulentic, J.W. Accretion onto Supermassive Black Holes in Quasars: Learning from Optical/UV Observations. In *New Developments in Black Hole Research*; Kreidler, P.V., Ed.; Nova Press: New York, NY, USA, 2006; p. 123.
7. Sulentic, J.W. Toward a classification scheme for broad-line profiles in active galactic nuclei. *Astrophys. J.* **1989**, *343*, 54–65. [[CrossRef](#)]
8. Shen, Y.; Ho, L.C. The diversity of quasars unified by accretion and orientation. *Nature* **2014**, *513*, 210–213. [[CrossRef](#)] [[PubMed](#)]
9. Panda, S.; Czerny, B.; Adhikari, T.P.; Hryniewicz, K.; Wildy, C.; Kuraszkievicz, J.; Śniegowska, M. Modeling of the Quasar Main Sequence in the Optical Plane. *Astrophys. J.* **2018**, *866*, 115. [[CrossRef](#)]
10. Sulentic, J.; Marziani, P.; Zamfir, S. The Case for Two Quasar Populations. *Balt. Astron.* **2011**, *20*, 427–434.
11. Marziani, P.; Zamanov, R.K.; Sulentic, J.W.; Calvani, M. Searching for the physical drivers of eigenvector 1: Influence of black hole mass and Eddington ratio. *Mon. Not. R. Astron. Soc.* **2003**, *345*, 1133–1144. [[CrossRef](#)]
12. Marziani, P.; Sulentic, J.W. Highly accreting quasars: Sample definition and possible cosmological implications. *Mon. Not. R. Astron. Soc.* **2014**, *442*, 1211–1229. [[CrossRef](#)]
13. Abramowicz, M.A.; Czerny, B.; Lasota, J.P.; Szuszkiewicz, E. Slim accretion disks. *Astrophys. J.* **1988**, *332*, 646–658. [[CrossRef](#)]
14. Mineshige, S.; Kawaguchi, T.; Takeuchi, M.; Hayashida, K. Slim-Disk Model for Soft X-Ray Excess and Variability of Narrow-Line Seyfert 1 Galaxies. *Publ. Astron. Soc. Jpn.* **2000**, *52*, 499–508.
15. Sadowski, A. Slim accretion disks around black holes. *arXiv* **2011**, arXiv:1108.0396.
16. Sun, J.; Shen, Y. Dissecting the Quasar Main Sequence: Insight from Host Galaxy Properties. *Astrophys. J. Lett.* **2015**, *804*, L15. [[CrossRef](#)]
17. Panda, S.; Marziani, P.; Czerny, B. The Quasar Main Sequence Explained by the Combination of Eddington Ratio, Metallicity, and Orientation. *Astrophys. J.* **2019**, *882*, 79. [[CrossRef](#)]
18. Peterson, B.M.; Ferland, G.J. An accretion event in the Seyfert galaxy NGC 5548. *Nature* **1986**, *324*, 345–347. [[CrossRef](#)]
19. Marziani, P.; Sulentic, J.W. Evidence for a very broad line region in PG 1138+222. *Astrophys. J.* **1993**, *409*, 612–616. [[CrossRef](#)]
20. Sulentic, J.W.; Zwitter, T.; Marziani, P.; Dultzin-Hacyan, D. Eigenvector 1: An Optimal Correlation Space for Active Galactic Nuclei. *Astrophys. J.* **2000**, *536*, L5–L9. [[CrossRef](#)]
21. Wang, J.; Li, Y. Strong Response of the Very Broad H $\beta$  Emission Line in the Luminous Radio-quiet Quasar PG 1416-129. *Astrophys. J. Lett.* **2011**, *742*, L12. [[CrossRef](#)]
22. Punsly, B. Multi-epoch Observations of the Red Wing Excess in the Spectrum of 3C 279. *Astrophys. J. Lett.* **2013**, *762*, L25. [[CrossRef](#)]
23. Wolf, J.; Salvato, M.; Coffey, D.; Merloni, A.; Buchner, J.; Arcodia, R.; Baron, D.; Carrera, F.J.; Comparat, J.; Schneider, D.P.; et al. Exploring the diversity of Type 1 active galactic nuclei identified in SDSS-IV/SPIDERS. *Mon. Not. R. Astron. Soc.* **2020**, *492*, 3580–3601. [[CrossRef](#)]
24. Snedden, S.A.; Gaskell, C.M. The Case for Optically Thick High-Velocity Broad-Line Region Gas in Active Galactic Nuclei. *Astrophys. J.* **2007**, *669*, 126–134. [[CrossRef](#)]
25. Peterson, B.M.; Wandel, A. Keplerian Motion of Broad-Line Region Gas as Evidence for Supermassive Black Holes in Active Galactic Nuclei. *Astrophys. J.* **1999**, *521*, L95–L98. [[CrossRef](#)]
26. Peterson, B.M.; Ferrarese, L.; Gilbert, K.M.; Kaspi, S.; Malkan, M.A.; Maoz, D.; Merritt, D.; Netzer, H.; Onken, C.A.; Pogge, R.W.; et al. Central Masses and Broad-Line Region Sizes of Active Galactic Nuclei. II. A Homogeneous Analysis of a Large Reverberation-Mapping Database. *Astrophys. J.* **2004**, *613*, 682–699. [[CrossRef](#)]
27. Punsly, B.; Marziani, P.; Berton, M.; Kharb, P. The Extreme Red Excess in Blazar Ultraviolet Broad Emission Lines. *Astrophys. J.* **2020**, *903*, 44. [[CrossRef](#)]
28. Wang, J.M.; Du, P.; Brotherton, M.S.; Hu, C.; Songsheng, Y.Y.; Li, Y.R.; Shi, Y.; Zhang, Z.X. Tidally disrupted dusty clumps as the origin of broad emission lines in active galactic nuclei. *Nat. Astron.* **2017**, *1*, 775–783. [[CrossRef](#)]
29. Gaskell, C.M. Direct evidence for gravitational domination of the motion of gas within one light-week of the central object in NGC 4151 and the determination of the mass of the probable black hole. *Astrophys. J.* **1988**, *325*, 114–118. [[CrossRef](#)]
30. Corbin, M.R. QSO Broad Emission Line Asymmetries: Evidence of Gravitational Redshift? *Astrophys. J.* **1995**, *447*, 496. [[CrossRef](#)]
31. Popovic, L.C.; Vince, I.; Atanackovic-Vukmanovic, O.; Kubicek, A. Contribution of gravitational redshift to spectral line profiles of Seyfert galaxies and quasars. *Astron. Astrophys.* **1995**, *293*, 309–314.
32. Gavrilović, N.; Popović, L.Č.; Kollatschny, W. The gravitational redshift in the broad line region of the active galactic nucleus Mrk 110. In *IAU Symposium*; Karas, V., Matt, G., Eds.; Cambridge University Press: Cambridge, UK, 2007; Volume 238, pp. 369–370. [[CrossRef](#)]
33. Bon, N.; Bon, E.; Marziani, P.; Jovanović, P. Gravitational redshift of emission lines in the AGN spectra. *Astrophys. Space Sci.* **2015**, *360*, 7. [[CrossRef](#)]
34. Marziani, P.; Sulentic, J.W. Quasar Outflows in the 4D Eigenvector 1 Context. *Astron. Rev.* **2012**, *7*, 33–57.
35. Marziani, P.; Sulentic, J.W.; Stirpe, G.M.; Dultzin, D.; Del Olmo, A.; Martínez-Carballo, M.A. Blue outliers among intermediate redshift quasars. *Astrophys. Space Sci.* **2016**, *361*, 3. [[CrossRef](#)]
36. Leighly, K.M.; Moore, J.R. Hubble Space Telescope STIS Ultraviolet Spectral Evidence of Outflow in Extreme Narrow-Line Seyfert 1 Galaxies. I. Data and Analysis. *Astrophys. J.* **2004**, *611*, 107–124. [[CrossRef](#)]

37. Kaastra, J.S.; Kriss, G.A.; Cappi, M.; Mehdipour, M.; Petrucci, P.O.; Steenbrugge, K.C.; Arav, N.; Behar, E.; Bianchi, S.; Boissay, R.; et al. A fast and long-lived outflow from the supermassive black hole in NGC 5548. *Science* **2014**, *345*, 64–68. [[CrossRef](#)]
38. Fine, S.; Croom, S.M.; Bland-Hawthorn, J.; Pimblett, K.A.; Ross, N.P.; Schneider, D.P.; Shanks, T. The CIV linewidth distribution for quasars and its implications for broad-line region dynamics and virial mass estimation. *Mon. Not. R. Astron. Soc.* **2010**, *409*, 591–610. [[CrossRef](#)]
39. Whittle, M. The Narrowline Region of Active Galaxies-Part Two-Relations Between OIII Profile Shape and Other Properties. *Mon. Not. R. Astron. Soc.* **1985**, *213*, 33.
40. Bennert, N.; Falcke, H.; Schulz, H.; Wilson, A.S.; Wills, B.J. Size and Structure of the Narrow-Line Region of Quasars. *Astrophys. J.* **2002**, *574*, L105–L109. [[CrossRef](#)]
41. Komossa, S.; Xu, D.; Zhou, H.; Storchi-Bergmann, T.; Binette, L. On the Nature of Seyfert Galaxies with High [O III]  $\lambda$ 5007 Blueshifts. *Astrophys. J.* **2008**, *680*, 926–938. [[CrossRef](#)]
42. Zamanov, R.; Marziani, P.; Sulentic, J.W.; Calvani, M.; Dultzin-Hacyan, D.; Bachev, R. Kinematic Linkage between the Broad- and Narrow-Line-emitting Gas in Active Galactic Nuclei. *Astrophys. J.* **2002**, *576*, L9–L13. [[CrossRef](#)]
43. Marziani, P.; Martínez Carballo, M.A.; Sulentic, J.W.; Del Olmo, A.; Stirpe, G.M.; Dultzin, D. The most powerful quasar outflows as revealed by the Civ  $\lambda$ 1549 resonance line. *Astrophys. Space Sci.* **2016**, *361*, 29. [[CrossRef](#)]
44. Sulentic, J.W.; Marziani, P.; Zamanov, R.; Bachev, R.; Calvani, M.; Dultzin-Hacyan, D. Average Quasar Spectra in the Context of Eigenvector 1. *Astrophys. J.* **2002**, *566*, L71–L75. [[CrossRef](#)]
45. Marziani, P.; Sulentic, J.W.; Plauchu-Frayn, I.; del Olmo, A. Is Mg II 2800 a Reliable Virial Broadening Estimator for Quasars? *Astron. Astrophys.* **2013**, *555*, 89.
46. Marziani, P.; Sulentic, J.W.; Stirpe, G.M.; Zamfir, S.; Calvani, M. VLT/ISAAC spectra of the H $\beta$  region in intermediate-redshift quasars. III. H $\beta$  broad-line profile analysis and inferences about BLR structure. *Astron. Astrophys.* **2009**, *495*, 83–112. [[CrossRef](#)]
47. Marziani, P.; Sulentic, J.W.; Zamanov, R.; Calvani, M.; Dultzin-Hacyan, D.; Bachev, R.; Zwitter, T. An Optical Spectroscopic Atlas of Low-Redshift Active Galactic Nuclei. *Astrophys. J. Suppl. Ser.* **2003**, *145*, 199–211. [[CrossRef](#)]
48. Bon, N.; Marziani, P.; Bon, E.; Negrete, C.A.; Dultzin, D.; del Olmo, A.; D’Onofrio, M.; Martínez-Aldama, M.L. Selection of highly-accreting quasars. Spectral properties of Fe II<sub>opt</sub> emitters not belonging to extreme Population A. *Astron. Astrophys.* **2020**, *635*, A151. [[CrossRef](#)]
49. Padovani, P. The faint radio sky: Radio astronomy becomes mainstream. *Astron. Astrophys. Rev.* **2016**, *24*, 13. [[CrossRef](#)]
50. Padovani, P. Active Galactic Nuclei at All Wavelengths and from All Angles. *Front. Astron. Space Sci.* **2017**, *4*, 35. [[CrossRef](#)]
51. Sulentic, J.W.; Marziani, P.; del Olmo, A.; Dultzin, D.; Perea, J.; Alenka Negrete, C. GTC spectra of  $z \approx 2.3$  quasars: Comparison with local luminosity analogs. *Astron. Astrophys.* **2014**, *570*, A96. [[CrossRef](#)]
52. Vestergaard, M.; Peterson, B.M. Determining Central Black Hole Masses in Distant Active Galaxies and Quasars. II. Improved Optical and UV Scaling Relationships. *Astrophys. J.* **2006**, *641*, 689–709. [[CrossRef](#)]
53. Netzer, H. Bolometric correction factors for active galactic nuclei. *Mon. Not. R. Astron. Soc.* **2019**, *488*, 5185–5191. [[CrossRef](#)]
54. Kriss, G. Fitting Models to UV and Optical Spectral Data. *Astron. Data Anal. Softw. Syst. III* **1994**, *61*, 437.
55. Boroson, T.A.; Green, R.F. The Emission-Line Properties of Low-Redshift Quasi-stellar Objects. *Astrophys. J. Suppl. Ser.* **1992**, *80*, 109. [[CrossRef](#)]
56. Sulentic, J.W.; del Olmo, A.; Marziani, P.; Martínez-Carballo, M.A.; D’Onofrio, M.; Dultzin, D.; Perea, J.; Martínez-Aldama, M.L.; Negrete, C.A.; Stirpe, G.M.; et al. What does CIV $\lambda$ 1549 tell us about the physical driver of the Eigenvector quasar sequence? *Astron. Astrophys.* **2017**, *608*, A122. [[CrossRef](#)]
57. Marziani, P.; Dultzin-Hacyan, D.; D’Onofrio, M.; Sulentic, J.W. Arp 194: Evidence of Tidal Stripping of Gas and Cross-Fueling. *Astron. J.* **2003**, *125*, 1897–1907. [[CrossRef](#)]
58. Zamfir, S.; Sulentic, J.W.; Marziani, P.; Dultzin, D. Detailed characterization of H $\beta$  emission line profile in low- $z$  SDSS quasars. *Mon. Not. R. Astron. Soc.* **2010**, *403*, 1759. [[CrossRef](#)]
59. Azzalini, A.; Regoli, G. Some properties of skew-symmetric distributions. *Ann. Inst. Statist. Math.* **2012**, *64*, 857–879. [[CrossRef](#)]
60. Urry, C.M.; Padovani, P. Unified Schemes for Radio-Loud Active Galactic Nuclei. *Publ. Astron. Soc. Pac.* **1995**, *107*, 803. [[CrossRef](#)]
61. Denney, K.D.; Peterson, B.M.; Pogge, R.W.; Adair, A.; Atlee, D.W.; Au-Yong, K.; Bentz, M.C.; Bird, J.C.; Brokofsky, D.J.; Chisholm, E.; et al. Diverse Kinematic Signatures from Reverberation Mapping of the Broad-Line Region in AGNs. *Astrophys. J.* **2009**, *704*, L80–L84. [[CrossRef](#)]
62. Du, P.; Brotherton, M.S.; Wang, K.; Huang, Z.P.; Hu, C.; Kasper, D.H.; Chick, W.T.; Nguyen, M.L.; Maithil, J.; Hand, D.; et al. Monitoring AGNs with H $\beta$  Asymmetry. I. First Results: Velocity-resolved Reverberation Mapping. *Astrophys. J.* **2018**, *869*, 142. [[CrossRef](#)]
63. Barth, A.J.; Vogler, H.A.; Guo, H.; Treu, T.; Bennert, V.N.; Canalizo, G.; Filippenko, A.V.; Gates, E.; Hamann, F.; Joner, M.D.; et al. The Lick AGN Monitoring Project 2016: Velocity-resolved H $\beta$  Lags in Luminous Seyfert Galaxies. *Astrophys. J.* **2022**, *925*, 52. [[CrossRef](#)]
64. Sulentic, J.W.; Marziani, P. The Intermediate-Line Region in Active Galactic Nuclei: A Region “Præter Necessitatem”? *Astrophys. J.* **1999**, *518*, L9–L12. [[CrossRef](#)]
65. Netzer, H.; Marziani, P. The Effect of Radiation Pressure on Emission-line Profiles and Black Hole Mass Determination in Active Galactic Nuclei. *Astrophys. J.* **2010**, *724*, 318–328. [[CrossRef](#)]

66. Ferland, G.J.; Hu, C.; Wang, J.; Baldwin, J.A.; Porter, R.L.; van Hoof, P.A.M.; Williams, R.J.R. Implications of Infalling Fe II-Emitting Clouds in Active Galactic Nuclei: Anisotropic Properties. *Astrophys. J.* **2009**, *707*, L82–L86. [[CrossRef](#)]
67. Marziani, P.; Sulentic, J.W.; Negrete, C.A.; Dultzin, D.; Zamfir, S.; Bachev, R. Broad-line region physical conditions along the quasar eigenvector 1 sequence. *Mon. Not. R. Astron. Soc.* **2010**, *409*, 1033–1048. [[CrossRef](#)]
68. Baldwin, J.; Ferland, G.; Korista, K.; Verner, D. Locally Optimally Emitting Clouds and the Origin of Quasar Emission Lines. *Astrophys. J.* **1995**, *455*, L119. [[CrossRef](#)]
69. Korista, K.; Baldwin, J.; Ferland, G.; Verner, D. An Atlas of Computed Equivalent Widths of Quasar Broad Emission Lines. *Astrophys. J. Suppl. Ser.* **1997**, *108*, 401. [[CrossRef](#)]
70. Murray, N.; Chiang, J. Disk Winds and Disk Emission Lines. *Astrophys. J.* **1997**, *474*, 91. [[CrossRef](#)]
71. Proga, D.; Stone, J.M.; Drew, J.E. Radiation-driven winds from luminous accretion discs. *Mon. Not. R. Astron. Soc.* **1998**, *295*, 595–617. [[CrossRef](#)]
72. Laor, A.; Brandt, W.N. The Luminosity Dependence of Ultraviolet Absorption in Active Galactic Nuclei. *Astrophys. J.* **2002**, *569*, 641–654. [[CrossRef](#)]
73. Bischetti, M.; Piconcelli, E.; Vietri, G.; Bongiorno, A.; Fiore, F.; Sani, E.; Marconi, A.; Duras, F.; Zappacosta, L.; Brusa, M.; et al. The WISSH quasars project. I. Powerful ionised outflows in hyper-luminous quasars. *Astron. Astrophys.* **2017**, *598*, A122. [[CrossRef](#)]
74. Vietri, G. The LBT/WISSH quasar survey: Revealing powerful winds in the most luminous AGN. American Astronomical Society Meeting Abstracts#. 2017; Volume 229. Available online: <https://ui.adsabs.harvard.edu/abs/2017AAS...22930206V/abstract> (accessed on 14 February 2022).
75. Vietri, G.; Piconcelli, E.; Bischetti, M.; Duras, F.; Martocchia, S.; Bongiorno, A.; Marconi, A.; Zappacosta, L.; Bisogni, S.; Bruni, G.; et al. The WISSH quasars project. IV. Broad line region versus kiloparsec-scale winds. *Astron. Astrophys.* **2018**, *617*, A81. [[CrossRef](#)]
76. Cano-Díaz, M.; Maiolino, R.; Marconi, A.; Netzer, H.; Shemmer, O.; Cresci, G. Observational evidence of quasar feedback quenching star formation at high redshift. *Astron. Astrophys.* **2012**, *537*, L8. [[CrossRef](#)]
77. Monari, G.; Famaey, B.; Carrillo, I.; Piffl, T.; Steinmetz, M.; Wyse, R.F.G.; Anders, F.; Chiappini, C.; Janßen, K. The escape speed curve of the Galaxy obtained from Gaia DR2 implies a heavy Milky Way. *Astron. Astrophys.* **2018**, *616*, L9. [[CrossRef](#)]
78. Ganci, V.; Marziani, P.; D’Onofrio, M.; del Olmo, A.; Bon, E.; Bon, N.; Negrete, C.A. Radio loudness along the quasar main sequence. *Astron. Astrophys.* **2019**, *630*, A110. [[CrossRef](#)]
79. del Olmo, A.; Marziani, P.; Ganci, V.; D’Onofrio, M.; Bon, E.; Bon, N.; Negrete, A.C. Optical spectral properties of radio loud quasars along the main sequence. In *Nuclear Activity in Galaxies Across Cosmic Time*; Pović, M., Marziani, P., Masegosa, J., Netzer, H., Negu, S.H., Tessema, S.B., Eds.; Cambridge University Press: Cambridge, UK, 2021; Volume 356, pp. 310–313. [[CrossRef](#)]
80. D’Onofrio, M.; Marziani, P.; Chiosi, C. Past, present and Future of the Scaling Relations of Galaxies and Active Galactic Nuclei. *arXiv* **2021**, arXiv:2109.06301.
81. Kriss, G.A. Coordinated UV and X-ray Observations of AGN Outflows. American Astronomical Society Meeting Abstracts#. 2017; Volume 229. Available online: <https://ui.adsabs.harvard.edu/abs/2017AAS...22920901K/abstract> (accessed on 14 February 2022).